



HAL
open science

On the use of frictional dampers for flutter mitigation of a highly flexible wing

Roberto Alcorta, Benjamin Chouvion, Guilhem Michon, Olivier Montagnier

► To cite this version:

Roberto Alcorta, Benjamin Chouvion, Guilhem Michon, Olivier Montagnier. On the use of frictional dampers for flutter mitigation of a highly flexible wing. *International Journal of Non-Linear Mechanics*, 2023, 156, pp.104515. 10.1016/j.ijnonlinmec.2023.104515 . hal-04189698

HAL Id: hal-04189698

<https://hal.science/hal-04189698>

Submitted on 28 Aug 2023

HAL is a multi-disciplinary open access archive for the deposit and dissemination of scientific research documents, whether they are published or not. The documents may come from teaching and research institutions in France or abroad, or from public or private research centers.

L'archive ouverte pluridisciplinaire **HAL**, est destinée au dépôt et à la diffusion de documents scientifiques de niveau recherche, publiés ou non, émanant des établissements d'enseignement et de recherche français ou étrangers, des laboratoires publics ou privés.

On the use of frictional dampers for flutter mitigation of a highly flexible wing

Roberto Alcorta^a, Benjamin Chouvion^{a,*}, Guilhem Michon^b, Olivier Montagnier^a

^a*Centre de Recherche de l'Ecole de l'air (CREA), Ecole de l'air et de l'espace, 13661 Salon-de-Provence, France*

^b*Université de Toulouse, ICA, CNRS, ISAE-Supaero, 31400 Toulouse, France*

Abstract

The prospect of aeroelastic instability, leading to large-amplitude limit cycle oscillations, is of particular concern for the highly flexible wings of solar high-altitude long-endurance (HALE) aircraft. Among the different strategies of vibration control, passive mitigation through friction dampers stands out as a promising solution in this context. While this concept has been proposed previously, related studies systematically use simple two-degrees-of-freedom airfoil models. In this paper, a more realistic structural model involving a three-dimensional nonlinear beam description of a full wing is considered. A friction damper is installed at a specific location on the wing span, and the response to aerodynamic loads is investigated numerically. Comparisons of critical speed and limit cycle amplitudes with and without the damper suggest improved vibration mitigation with respect to a linear viscous damper.

Keywords: friction damper, flutter, geometric nonlinearities, highly flexible wing, HALE drone

1. Introduction

Solar high-altitude long-endurance (HALE) pseudo-satellites are an emerging trend which involves deploying Unmanned Air Vehicles (UAV) in stratospheric flight. These are able to carry out missions typically attributed to conventional satellites. However, these vehicles are subjected to a specific set of design constraints in order to achieve their intended purpose, which includes a very high energy efficiency and a light frame. The resulting structures involve flexible wings with high aspect ratios, particularly prone to dynamic instabilities such as aeroelastic flutter. This phenomenon leads to limited flight domains and performances of current solar HALE UAVs designs [1]. Therefore, a proper prediction and control of flutter is critical to

*Corresponding author

Email address: benjamin.chouvion@ecole-air.fr (Benjamin Chouvion)

guarantee safe and robust operation of solar HALE UAVs. Several computations tools are available for this
10 matter, for instance: NATASHA [2], UM/NAST [3], SharPy [4] and GEBTAero [5]. They all use unsteady
potential theories (strip theory or lifting surface) as aerodynamic modeling.

Different solutions of active aeroelastic control have been investigated to prevent undesirable vibrations
and mitigate flutter effects [6]. Passive control is another strategy to limit detrimental large-amplitude Limit
Cycle Oscillations (LCOs) and postpone instability. Adding a nonlinear energy absorber has also been
15 considered theoretically [7, 8], and experimentally [9]. Friction damping is another vibration mitigation
technique for wing [10], or fan blades [11]. Those studies addressed simplistic reduced models focused
on an airfoil section and a limited numbers of DOF (Degrees of Freedom); the main reason being that
the damper parameterization involves usually an analytical approach. Continuous and more realistic wing
models require specific attention both on the structural modeling and damper design fronts. The former,
20 owing to the high flexibility of solar HALE wings, must include geometrical nonlinearities to cope with
large displacements and rotations, thereby enabling quantitative analyses of LCOs. In turn, this information
can be used to design effective dampers for fluttering wings whose vibration amplitudes must be kept small
past the critical speed. Moreover, in the particular context of HALE UAV's required to operate at low energy
consumption, an efficient and carefully-designed passive control strategy is of highly desirable.

25 For a high-aspect-ratio wing, using a nonlinear beam model in place of a full three-dimensional finite
element model is convenient. The latter would allow to run complex simulations on a realistic geometry, but
the treatment of distributed nonlinearities requires specialized reduction methods to be practical ([12] for
instance). A beam model benefits from an inherently smaller size and can be discretized straightforwardly
through the use of a Rayleigh-Ritz approach [13, 14]. Geometrically exact beam models with specific
30 rotation parameterization have been developed to deal with arbitrarily large displacements and rotations,
e.g. [15] or [16], but for moderate cases the use of simplified models leads to reasonable accuracy.

The objective of the paper is to investigate the potential benefit of friction damping for flutter control of a
nonlinear flexible wing. The wing is represented mathematically by a geometrically approximate nonlinear
beam model, described in detail in Sect. 2 and validated in Sect. 3. Numerical investigations on the critical
35 velocity and LCOs amplitude function of the friction damper characteristics are presented in Sect. 4. Finally,
discussion of results and perspectives for future work are the subject of Sect. 5.

2. Modeling

In this section, the nonlinear equations of motion are obtained by using the following extended Euler-Lagrange equations on a Rayleigh-Ritz discretization of the continuous dynamic variables:

$$\frac{d}{dt} \left(\frac{\partial (\mathcal{T}_{\text{tot}} - \mathcal{U}_{\text{tot}})}{\partial \dot{q}_j} \right) + \frac{\partial \mathcal{D}}{\partial \dot{q}_j} - \frac{\partial (\mathcal{T}_{\text{tot}} - \mathcal{U}_{\text{tot}})}{\partial q_j} - \frac{\partial \mathcal{W}_{\text{aero}}}{\partial q_j} = 0 \quad , \quad \forall j \in [1, \dots, N_t] . \quad (1)$$

40 In (1), N_t is the total number of unknown generalized coordinates; \mathcal{T}_{tot} and \mathcal{U}_{tot} are, respectively, the total kinetic and potential energies; $\mathcal{W}_{\text{aero}}$ is the work developed by aerodynamic forces; and \mathcal{D} is the dissipated energy. The equation of motion obtained is discussed in Sect. 2.4.

2.1. Structural model

The wing model presented here is based on the work by [17]. Therein, the authors considered a pre-
 45 twisted and pre-bent rotor blade, and developed a formulation in which the different blade displacements are nonlinearly coupled. Such an approach is similar to that of [18] and [14], among others. These models, however, tend to discard important nonlinear stiffness terms arising from moderate-to-large local rotations, and thus provide low accuracy in the case of very flexible wings. Consequently, an appropriate extension is considered here, thus placing the proposed model between the ones of [18] and an exact formulation (see,
 50 e.g., [15]) in terms of accuracy. An initially-straight beam is considered in this paper for simplicity.

2.1.1. Beam kinematics

Let $\mathcal{B}_0 = (O, x, y, z)$ be a global coordinate system at whose origin O is clamped a long, slender wing. The x -axis is oriented along the undeformed wing's elastic axis and the y -axis points towards the leading edge, see Fig. 1. The wing's deformed state is characterized by the displacements $u(x, t)$, $v(x, t)$ and $w(x, t)$ of the
 55 elastic axis, and the twist angle $\phi(x, t)$ about the (deformed) elastic axis x^* (see Fig. 2). For conciseness, dependency of these variables on x and t will not be shown explicitly hereafter.

Finally, let define a local coordinate system $\mathcal{B}_d = (P', \xi, \eta, \zeta)$ associated with the deformed configuration. Its ξ -axis is tangential to the deformed elastic axis x^* and its η -axis is parallel to the local chord. The rotation from the \mathcal{B}_0 -frame to the \mathcal{B}_d -frame is expressed with the transformation matrix $\mathbf{T}(x, t)$ (given in
 60 Appendix A). \mathbf{T} can be computed as the result of three successive rotations about the Euler angles ψ , θ and $\hat{\phi}$, shown in Fig. 3. Note that the twist angle ϕ , used as dynamic variable, is not the same as $\hat{\phi}$ [14].

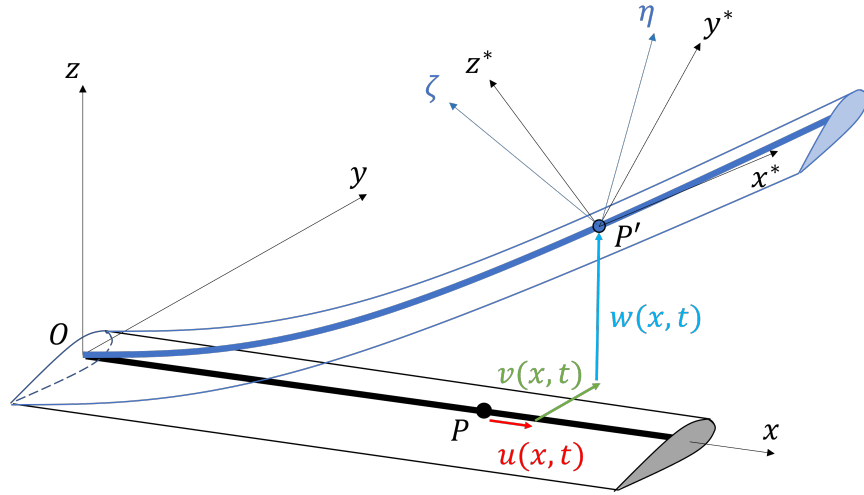


Figure 1: Wing model: initial and deformed states.

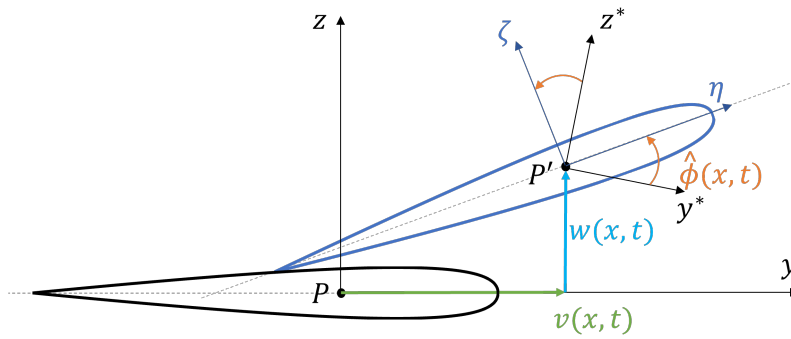


Figure 2: Local coordinate system $\mathcal{B}_d = (P', \xi, \eta, \zeta)$. The axes x and x^* are shown parallel in this figure but they should not be in a three-dimensional deformation.

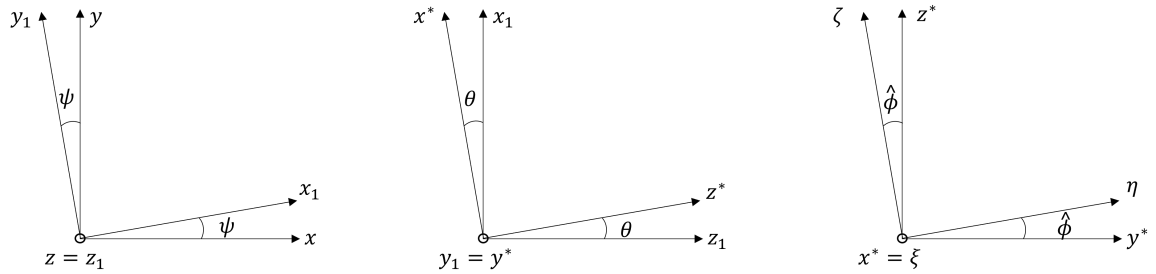


Figure 3: Euler angles defining the rotation matrix \mathbf{T} from the \mathcal{B}_0 -frame to the deformed \mathcal{B}_D -frame.

Using these definitions, the position \mathbf{r}_0 of an arbitrary point on the wing in its undeformed configuration is:

$$\mathbf{r}_0(x, \eta, \zeta) \Big|_{\mathcal{B}_0} = \begin{bmatrix} x \\ 0 \\ 0 \end{bmatrix}_{\mathcal{B}_0} + \mathbf{T}_0^T(x) \begin{bmatrix} 0 \\ \eta \\ \zeta \end{bmatrix}_{\mathcal{B}_d} = \begin{bmatrix} x \\ \eta \\ \zeta \end{bmatrix}_{\mathcal{B}_0}, \quad (2)$$

where \mathbf{r}_0 is expressed in the global coordinate system. $\mathbf{T}_0(x)$ corresponds to the rotation matrix evaluated for $u = v = w = \phi = 0$. \bullet^T denotes the transpose matrix.

The position of the same material point after deformation, \mathbf{r} , is then:

$$\mathbf{r}(x, \eta, \zeta, t) \Big|_{\mathcal{B}_0} = \begin{bmatrix} x + u \\ v \\ w \end{bmatrix}_{\mathcal{B}_0} + \mathbf{T}^T(x, t) \begin{bmatrix} 0 \\ \eta \\ \zeta \end{bmatrix}_{\mathcal{B}_d}. \quad (3)$$

The expression (3) neglects cross-sectional warping, which is justified in the case of a high-aspect-ratio wing under no axial loading [19].

2.1.2. Energy derivations

Assuming a linearly elastic material, and the hypotheses of Euler-Bernoulli beam theory, the wing's elastic potential energy is:

$$\mathcal{U} = \frac{1}{2} \int_0^L \int_A \left(E \varepsilon_{xx}^2 + G \gamma_{x\eta}^2 + G \gamma_{x\zeta}^2 \right) d\eta d\zeta dx, \quad (4)$$

where E and G are the material's Young's and shear modulus, respectively. A is the cross-section area and L the wing length. Furthermore, using the definition of \mathbf{r}_0 (Eq. (2)) and \mathbf{r} (Eq. (3)), the strain components $(\varepsilon_{xx}, \gamma_{x\eta}, \gamma_{x\zeta})$ may be expressed as functions of the local extension e_ξ and curvatures $(\kappa_\xi, \kappa_\eta, \kappa_\zeta)$, as follows:

$$\varepsilon_{xx} = e_\xi + \eta \kappa_\zeta - \zeta \kappa_\eta, \quad (5a)$$

$$\gamma_{x\eta} = \kappa_\xi \zeta, \quad (5b)$$

$$\gamma_{x\zeta} = -\kappa_\xi \eta, \quad (5c)$$

where quadratic terms in the extension and curvatures have been neglected by assuming small strains. By definition, the axial extension is given by:

$$e_\xi = \sqrt{(1 + u')^2 + v'^2 + w'^2} - 1. \quad (6)$$

On the other hand, an expression for the curvatures is found through Kirchoff's kinetic analogy [20], which implies: $\mathbf{T}' \equiv \partial(\mathbf{T})/\partial x = \mathbf{D}\mathbf{T}$ where \mathbf{D} is the so-called *spin tensor*, a skew-symmetric matrix defined by the property: $\mathbf{D}\mathbf{v} = [\kappa_\xi, \kappa_\eta, \kappa_\zeta]^\top \wedge \mathbf{v}, \forall \mathbf{v} \in \mathbb{R}^3$. It follows that $\mathbf{D} = \mathbf{T}'\mathbf{T}^\top$, which provides a set of equations for the curvatures. With \mathbf{T} detailed in [Appendix A](#), it leads to:

$$\kappa_\xi = -\hat{\phi}' + \sin(\theta)\psi', \quad (7a)$$

$$\kappa_\eta = -\theta' \cos(\hat{\phi}) - \cos(\theta) \sin(\hat{\phi})\psi', \quad (7b)$$

$$\kappa_\zeta = \theta' \sin(\hat{\phi}) - \cos(\theta) \cos(\hat{\phi})\psi', \quad (7c)$$

where $\bullet' = \partial \bullet / \partial x$. From geometrical considerations, one may express the derivatives and trigonometric functions of Euler angles appearing in (7) purely in terms of the dynamic variables (u, v, w, ϕ) and their derivatives (see [Appendix A](#)). Incorporating these definitions into Eq. 4 and performing integration over the beam's cross-section leads to the following expression for elastic potential energy:

$$\begin{aligned} \mathcal{U} = \frac{1}{2} \int_0^L & \left(EAe_\xi^2 + EI_\eta \kappa_\eta^2 + EI_\zeta \kappa_\zeta^2 + GJ\kappa_\xi^2 + \right. \\ & \left. - 2EAd_\zeta e_\xi \kappa_\eta + 2EAd_\eta e_\xi \kappa_\zeta - 2EI_{\eta\zeta} \kappa_\eta \kappa_\zeta \right) dx. \end{aligned} \quad (8)$$

with the usual definitions for the coefficients:

$$\begin{aligned} EA &= \int_A E d\eta d\zeta, & EAd_\eta &= \int_A E\eta d\eta d\zeta, & EAd_\zeta &= \int_A E\zeta d\eta d\zeta, \\ EI_\eta &= \int_A E\zeta^2 d\eta d\zeta, & EI_\zeta &= \int_A E\eta^2 d\eta d\zeta, & EI_{\eta\zeta} &= \int_A E\eta\zeta d\eta d\zeta, \\ GJ &= \int_A G(\eta^2 + \zeta^2) d\eta d\zeta. \end{aligned}$$

In Eq. (8), E and G do not need to be constant over a cross-section. Moreover, this equation is also valid for a wing with varying cross-section, as these coefficients could be functions of x . Next, potential energy is expanded as a Taylor series in order to obtain third-order accurate strains. The crucial difference between the proposed and cited models is that, having expressed potential energy in the invariant form of Eq. (8) a consistent third-order approximation can be achieved by expanding curvatures to as high an order as required, and only then truncating terms in the energy expression. For this, the ordering scheme proposed by [17] and summarized in Table (1) is used.

x/L	$O(1)$	u/L	$O(\varepsilon^2)$
v/L	$O(\varepsilon)$	w/L	$O(\varepsilon)$
ϕ	$O(\varepsilon)$		

Table 1: Orders of magnitude, compared to a small and dimensionless parameter ε .

Ultimately, Eq. (7) is rewritten as:

$$\kappa_\xi = -\hat{\phi}' - v''w' \equiv -\phi', \quad (9a)$$

$$\kappa_\eta = w'' \left(1 + \frac{w'^2}{2} - \frac{\phi^2}{2} \right) - v'' \left(\phi - \int_0^x v''w' dx \right) + O(\varepsilon^4), \quad (9b)$$

$$\kappa_\zeta = v'' \left(-1 + v'^2 + \frac{w'^2}{2} + \frac{\phi^2}{2} + u' \right) - w'' \left(\phi - \int_0^x v''w' dx \right) + v'u'' + O(\varepsilon^4), \quad (9c)$$

95 which is valid for moderate rotations and torsion angles. The relationship between the Euler angle $\hat{\phi}$ and the twist angle ϕ is established in Eq. (9a). The third-order terms $v''v'^2/2$ and $w''w'^2/2$ in the above equations are frequently omitted, as in [17], which leads to equations of motion lacking nonlinear bending stiffness terms and hence unable to correctly represent beam motions in the large displacement scenario. Similarly, the exact definition of e_ξ (see (6)) is expanded to yield:

$$e_\xi = u' + \frac{1}{2}(v'^2 + w'^2) + O(\varepsilon^4). \quad (10)$$

100 Inserting Eqs. (9) and (10) into the potential energy, Eq. (8), leads to an expression solely in terms of the four dynamic variables (u, v, w, ϕ) .

In addition, one might include gravitational potential energy through the term:

$$\mathcal{U}_g = - \int_0^L \int_A \rho g w(x, t) d\eta d\zeta dx, \quad (11)$$

where ρ is the material density and g the acceleration due to gravity. Once the total potential energy has been computed, terms of order higher than $O(\varepsilon^4)$ are neglected.

105 The kinetic energy of the wing is straightforwardly computed with the relation:

$$\mathcal{T} = \frac{1}{2} \int_0^L \int_A \rho \left(\frac{\partial \mathbf{r}}{\partial t} \right) \cdot \left(\frac{\partial \mathbf{r}}{\partial t} \right) d\eta d\zeta dx.$$

By substituting the value of \mathbf{r} from Eq. (3) and expressing the Euler angles as a function of the dynamic variables, the energy, with terms up to second order, becomes:

$$\mathcal{T} = \frac{1}{2} \int_0^L (m(\dot{u}^2 + \dot{v}^2 + \dot{w}^2) + mk_t^2 \dot{\phi}^2 + 2m\dot{\phi}(e_\eta \dot{w} - e_\zeta \dot{v})) dx, \quad (12)$$

where $\dot{\bullet} = \partial \bullet / \partial t$ and

$$\begin{aligned} m &= \int_A \rho \, d\eta \, d\zeta, & k_t^2 &= \frac{1}{m} \int_A \rho (\eta^2 + \zeta^2) \, d\eta \, d\zeta, \\ e_\eta &= \frac{1}{m} \int_A \rho \eta \, d\eta \, d\zeta, & e_\zeta &= \frac{1}{m} \int_A \rho \zeta \, d\eta \, d\zeta. \end{aligned}$$

The kinetic energy (12) has been truncated at $O(\varepsilon^2)$ whereas terms up to order $O(\varepsilon^4)$ were kept in the
110 potential energy (8) because their orders of magnitude are such that $\mathcal{T}/\mathcal{U} = O(\varepsilon^2)$ (see, e.g., [18]). As
before, the coefficients in (12) are allowed to vary along the beam's span. Contrary to what is given in [17],
the kinetic energy (12) accounts for possible asymmetric cross-section with respect to the η -axis.

2.2. Aerodynamic forces

For the purposes of this paper, a simple linear quasi-steady model based on strip theory is considered for
115 the aerodynamic forces. Indeed, as seen in following sections, such a model is sufficient to induce flutter for
certain configurations, and thus allows to assess the effectiveness of the friction-damper concept proposed
here.

The virtual work done by aerodynamic forces is defined as:

$$\delta \mathcal{W}'_{\text{aero}} = \int_0^L (\delta v F_y + \delta w F_z + \delta \phi M_\xi) \, dx, \quad (13)$$

where F_y and F_z are the components of the aerodynamic forces per unit length expressed in the global frame,
120 and M_ξ is the aerodynamic moment along the ξ -axis expressed at the airfoil's elastic center, noted P' , located
at a distance x_A from its aerodynamic center, noted A . The work done by the axial aerodynamic force has
been neglected in (13).

The aerodynamic forces (F_y, F_z) and moment M_ξ will be calculated next with respect to the lift force
 L , drag force D , and aerodynamic moment M_0 in A , illustrated in Fig. 4. At any given section along the
125 wing's span, L and D are defined in the perpendicular and tangent directions, respectively, of $\mathbf{U}_{P'}$, the linear
airfoil velocity at P' (see Fig. 4) relative to the airflow. Assuming small angles of attack, they are defined by
classical strip theory as:

$$D = \frac{1}{2} \rho_\infty c \|\mathbf{U}_M\|^2 C_{d0}, \quad (14a)$$

$$L = \frac{1}{2} \rho_\infty c \|\mathbf{U}_M\|^2 (C_{l0} + C_{l\alpha} \alpha_{\text{eff}}). \quad (14b)$$

In Eq. (14), α_{eff} is the effective angle of attack; ρ_∞ is the air density; c is the airfoil chord length; and
 C_{l0} , $C_{l\alpha}$ and C_{d0} are dimensionless aerodynamic coefficients. \mathbf{U}_M is the velocity of the three-quarter chord

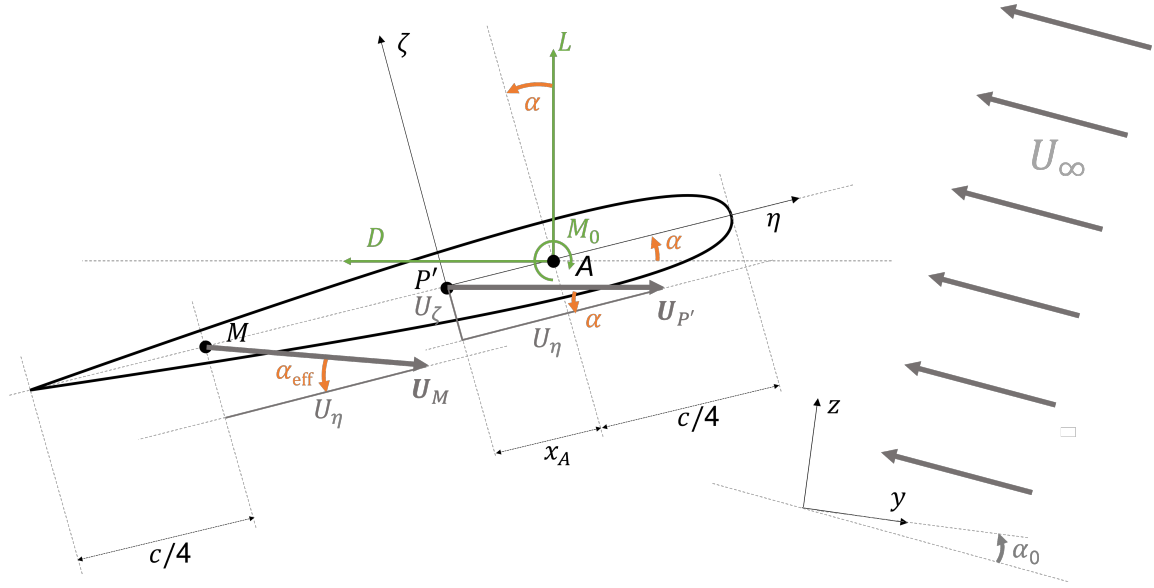


Figure 4: Aerodynamic forces and moment on an airfoil. Note that the airfoil plane (η, ζ) is not necessarily the same as the plane (y, z) .

130 point, noted M in Fig. 4, relatively to the airflow [21]. Let assume that the wing is immersed in a steady airflow of speed $-U_\infty$ whose direction defines a steady angle of attack α_0 between the airfoil profile and the undeformed global y -axis, see Fig. 4. \mathbf{U}_M is then given by:

$$\mathbf{U}_M \Big|_{\mathcal{B}_d} = \mathbf{U}_{P'} \Big|_{\mathcal{B}_d} + \begin{bmatrix} 0 \\ 0 \\ (x_A - \frac{c}{2}) \dot{\alpha} \end{bmatrix} \Big|_{\mathcal{B}_d}, \quad (15)$$

where $\mathbf{U}_{P'}$ accounts for both the wing linear motion and the airflow speed, and is defined by:

$$\mathbf{U}_{P'} \Big|_{\mathcal{B}_d} = \mathbf{T} \begin{bmatrix} \dot{u} \\ \dot{v} + U_\infty \cos \alpha_0 \\ \dot{w} - U_\infty \sin \alpha_0 \end{bmatrix} \Big|_{\mathcal{B}_0} \equiv \begin{bmatrix} U_\xi \\ U_\eta \\ U_\zeta \end{bmatrix} \Big|_{\mathcal{B}_d}. \quad (16)$$

In Eq. (15), $\dot{\alpha}$ corresponds to the airfoil angular velocity about the deformed elastic axis and is given by:

$$\dot{\alpha} = -\dot{\hat{\phi}} - \dot{v}'w' + O(\varepsilon^4) = -\dot{\hat{\phi}} + \int_0^x [\dot{w}'v'' - \dot{v}'w''] dx + O(\varepsilon^4) \quad (17)$$

135 whose mathematical form closely resembles Eq. (9a) for κ_ξ , as expected from Kirchoff's kinetic analogy.

In Eq. (14), the effective angle of attack α_{eff} is defined as the angle between \mathbf{U}_M and the chord-wise η -axis direction. With the assumption of small α_{eff} , Eqs. (15) and (16) give:

$$\tan(\alpha_{\text{eff}}) = \frac{-U_\zeta + (\frac{c}{2} - x_A)\dot{\alpha}}{U_\eta} \approx \alpha_{\text{eff}}. \quad (18)$$

With the same assumption and considering $U_\eta \gg (U_\zeta, U_\xi)$, the quantity $\|\mathbf{U}_M\|^2$ can be approximated to U_η^2 , which then simplifies Eq. (14) to:

$$D = \frac{1}{2}\rho_\infty c U_\eta^2 C_{d0}, \quad (19a)$$

$$L = \frac{1}{2}\rho_\infty c U_\eta \left(C_{l0} U_\eta + C_{l\alpha} (-U_\zeta + (\frac{c}{2} - x_A)\dot{\alpha}) \right). \quad (19b)$$

140 The aerodynamic forces (F_y, F_z) expressed in the global frame \mathcal{B}_0 are obtained from D and L through a rotation of angle α about P' followed by a rotation from the \mathcal{B}_d -frame to the \mathcal{B}_0 -frame characterized with the \mathbf{T} -matrix. This gives :

$$\begin{bmatrix} - \\ F_y \\ F_z \end{bmatrix}_{\mathcal{B}_0} = \mathbf{T}^T \left(\begin{bmatrix} 1 & 0 & 0 \\ 0 & \cos(\alpha) & \sin(\alpha) \\ 0 & -\sin(\alpha) & \cos(\alpha) \end{bmatrix} \begin{bmatrix} 0 \\ -D \\ L \end{bmatrix}_{\mathcal{B}_d} \right). \quad (20)$$

To simplify the expressions, the zero-lift moment is assumed to be null ($M_0 = 0$). Thus, the total moment M_ξ in P' only involves the moments generated by the drag and lift forces and by the centrifugal part of non-circulatory lift, which is $\rho_\infty C_{l\alpha} c^2 U_\eta \dot{\alpha} / 8$, through the moment arm $-c/4$ (see [21] for details). Hence:

$$M_\xi = x_A \left(D \sin(\alpha) + L \cos(\alpha) \right) - \rho_\infty C_{l\alpha} \frac{c^3}{32} U_\eta \dot{\alpha}. \quad (21)$$

Finally, substituting Eq. (19) into Eqs. (20) and (21), making the assumption of $\cos \alpha \approx 1$ and $\sin \alpha \approx -U_\zeta / U_\eta$, and developing the \mathbf{T} -matrix in Eqs. (15) and (20) as a function of the variables (u, v, w, ϕ) (see [Appendix A](#)) give an expression of the aerodynamic forces F_y, F_z and moment M_ξ solely in terms of (u, v, w, ϕ) , their time derivative and the airflow velocity U_∞ . Eqs. (20) and (21) are then substituted into (13) to express the work done by aerodynamic forces solely as a function of the kinematic variables and U_∞ . The equation obtained is finally considered in the Euler-Lagrange equations (1) to create stiffness and damping terms induced by aeroelastic effects. As for the structural model, nonlinear aeroelastic terms up to $O(\varepsilon^3)$ are kept. The non-linearity introduced due to both large displacement and three-dimensional kinematics amounts to treating lift and drag as follower forces rather than them having a fixed direction in space, which is crucial in a large-displacement context.

2.3. Friction damper

Let consider a damper attached to the wing at a location $x = x_D$, as illustrated in Fig. 5. The technological implementation of this device is assumed to only allow vertical displacements of the damper, noted $z_D(t)$, along the global z -axis. Possible inclination of the damper system under wing large rotation is thus neglected. The damper consists of a point mass m_D connected to the wing by a linear stiffness k_D and a sliding contact.

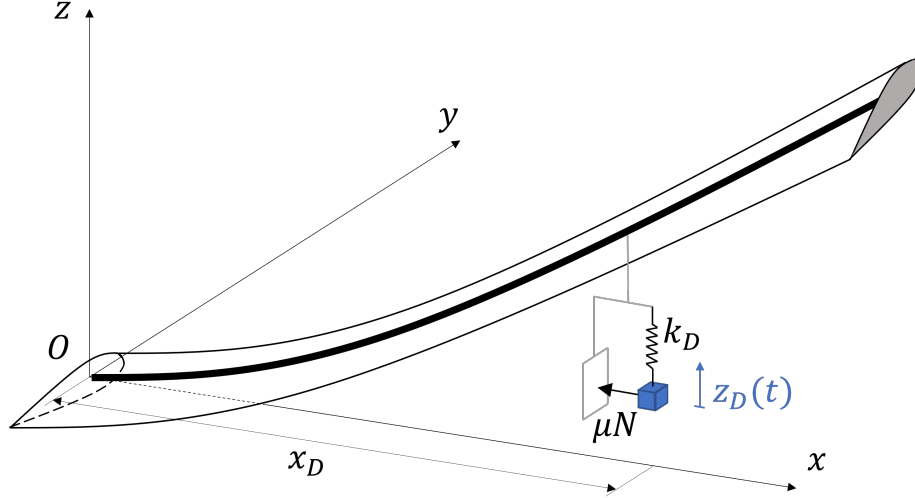


Figure 5: Schematic diagram of the tuned mass frictional damper.

160

The later is modeled by a smooth approximation of dry (Coulomb) friction such that the friction force f_f is:

$$f_f(t) = \mu N \tanh\left(\frac{\dot{w}(x_D, t) - \dot{z}_D(t)}{\varepsilon}\right), \quad (22)$$

where μN , regarded as a single coefficient, express the normal force at the contact interface multiplied by the friction coefficient, and ε is a regularization parameter.

The potential, kinetic and dissipated energies associated with the damper system are then respectively
 165 given by:

$$\mathcal{U}_d = \frac{k_D}{2} (w(x_D, t) - z_D(t))^2 \quad \mathcal{T}_d = \frac{m_D}{2} \dot{z}_D^2(t) \quad \mathcal{D}_d = (\dot{w}(x_D, t) - \dot{z}_D(t)) f_f(t)$$

These expressions are added to energies of the overall system when using the Euler-Lagrange equations (1).

2.4. Discretization and equations of motion

Each continuous variable (u, v, w, ϕ) is approximated with the following Rayleigh-Ritz discretization:

$$f(x, t) = \sum_{j=1}^{N_f} \varphi_{fj}(x) q_{fj}(t) \quad (23)$$

where f is a placeholder for any one of the variables (u, v, w, ϕ) , q_{fj} are the unknown generalized coordinates and φ_{fj} are associated shape functions. In order for the shape functions to be kinematically admissible, they are required to satisfy the geometric boundary conditions at $x = 0$:

$$\begin{aligned} \varphi_{uj}(0) &= 0 & \forall j \in [1, \dots, N_u] \\ \varphi_{vj}(0) &= \varphi'_{vj}(0) = 0 & \forall j \in [1, \dots, N_v] \\ \varphi_{wj}(0) &= \varphi'_{wj}(0) = 0 & \forall j \in [1, \dots, N_w] \\ \varphi_{\phi j}(0) &= 0 & \forall j \in [1, \dots, N_\phi]. \end{aligned}$$

A multitude of options are possible for the choice of shape functions. In this paper, a power series expansion of the following form is used:

$$\varphi_{fj}(x) = \left(\frac{x}{L}\right)^{a+j} \quad (24)$$

with $a = 0$ for φ_{uj} and $\varphi_{\phi j}$, and $a = 1$ otherwise. Such functions have been successfully employed in previous studies (see, e.g., [17] or [13]) and constitute a good alternative to linear eigenmodes, which are a popular choice in dynamics problems but are known to be sub-optimal in the present context [22]. In any case, the number of shape functions required to achieve convergence – with regards to an appropriate metric – must be studied carefully. Such a study is conducted in Sect. 3. Discretization using finite elements is also a possible option and useful to easily couple the nonlinear beam with another structure (see, e.g., in [23]), however it generally requires more degrees of freedom to obtain a similar accuracy on the low-order modes.

The $N_t = N_u + N_v + N_w + N_\phi + 1$ discrete equations of motion are finally obtained by replacing the continuous variables (u, v, w, ϕ) by their expressions in (23) within the work and energy terms, computing integrals over the wing span, and applying Eq. (1). This yields to the system of equations:

$$\mathbf{M}\ddot{\mathbf{q}} + \mathbf{C}\dot{\mathbf{q}} + \mathbf{K}\mathbf{q} + \mathbf{f}_{\text{NL}}(\mathbf{q}, \dot{\mathbf{q}}) + \mathbf{f}_{\text{aero}}(\mathbf{q}, \dot{\mathbf{q}}, U_\infty) = \mathbf{f}_{\text{ext}}, \quad (25)$$

where all generalized coordinates are contained in a single vector \mathbf{q} such that:

$$\mathbf{q}(t) = [\mathbf{q}_u^T(t), \mathbf{q}_v^T(t), \mathbf{q}_w^T(t), \mathbf{q}_\phi^T(t), z_D(t)]^T.$$

185 In Eq. (25), \mathbf{M} and \mathbf{K} are respectively the generalized mass and stiffness matrices. Linear damping has been included into the model via the matrix \mathbf{C} . Modal damping calculated on the underlying linear autonomous system of (25) will be used in Section 4. The term \mathbf{f}_{NL} contains the nonlinear contributions stemming from geometrical and frictional effects. Aeroelastic effects are grouped in vector \mathbf{f}_{aero} function of airflow velocity U_∞ . It contains, to third order in the generalized displacements, a non-zero constant term (solely) for $\alpha_0 \neq 0$ and linear, quadratic and cubic terms in $(\mathbf{q}, \dot{\mathbf{q}})$. \mathbf{f}_{ext} groups state-independent generalized forces, which are
 190 solely produced by gravity in this case (see Eq. (11)).

The model described above has been implemented as a MATLAB toolbox named HiFleW (for Highly Flexible Wing), to which references are made throughout the remainder of this paper.

3. Model Validation

195 The aim of this section is to validate the HiFleW toolbox described previously by examining the response of the structure without the added damper in different typical loading scenarios. To this end, test cases were chosen on the basis of two criteria: quantitative results available in the literature, and adequacy for direct comparison to the proposed model ¹ .

3.1. Static test case accounting for geometric nonlinear effects

200 An uniform, straight beam with constant (rectangular) cross-section is considered. Its dimension and material properties follow that of [24]: the beam length, width and thickness are respectively 40 cm, 25 mm and 0.4 mm. The material's Young's modulus is 194.3 Gpa and its density is 7726.8 kg/m³. Ignoring aerodynamic loading, the beam is first subjected to both its own weight and that of an additional 10 g point mass added at its tip. The nonlinear static equilibrium equation, given by (25) with $\ddot{\mathbf{q}} = \dot{\mathbf{q}} = \mathbf{0}$, is numerically
 205 solved with a Newton-Raphson algorithm.

Since a discretization approach is used, the deformed shape at equilibrium varies with the chosen type and number of shape functions, until convergence is achieved. Let consider, for instance, the Chebyshev polynomials proposed in [13], modified to satisfy the fixed boundary condition at $x = 0$. Fig. 6 shows the evolution of the beam tip displacements with increasing number of shape functions N , with $N_u = N_v = N_w =$
 210 $N_\phi = N$, for both Chebyshev and power-series approximations (see (24)). The physical displacements have

¹This rules out, in particular, models which implement a more detailed aerodynamic description, e.g., unsteady effects, which are out of scope for the present paper.

been reconstructed from the generalized variables through Eq. (23). Despite the added richness of Chebyshev polynomials, these results indicate that a power-series expansion has virtually the same convergence rate. This implies that the latter could be used equivalently without sacrificing the solution quality, which is convenient due to their ease of mathematical manipulation.

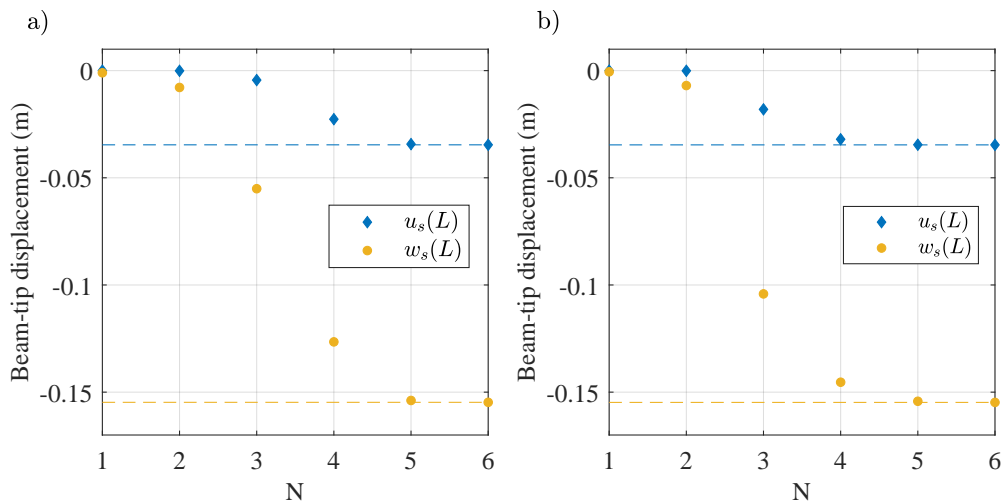


Figure 6: Static deformation convergence for different shape function types: a) Chebyshev polynomials, b) power series.

Concerning the converged numerical values obtained, these highlight two noteworthy features: firstly, the static vertical displacement is $w_s(L) = -154.8$ mm, which amounts to approximately 39% of the total beam span; secondly, a non-zero axial displacement is present at the beam tip, although its amplitude is small in comparison to the former: $u_s(L) = -34.6$ mm. These effects arise from the highly-flexible nature of the chosen beam and from the nonlinear coupling terms in the equations of motion. Following the convergence analysis shown in Fig. 6, power-series discretization with $N = 6$ will be used in the remaining of this paper. It should be noted that, while these numbers have been shown to be sufficient with respect to static deformation, a dynamic analysis also requires that the chosen number of functions is enough to accurately reconstruct the vibration modes of interest. This will be illustrated in Sect. 3.2.

In Fig. 7, the static deformation obtained by HiFleW is compared to a Nonlinear Finite Element (NLFE) computation using ABAQUS². Two versions of the former are considered: both neglecting and including

²The NLFE model consists of a geometrically nonlinear beam meshed with 100 Euler-Bernoulli beam elements.

the cubic terms in the curvature definitions, Eq. (7). The first corresponds to linearized rotations, while the second takes into account large rotation effects.

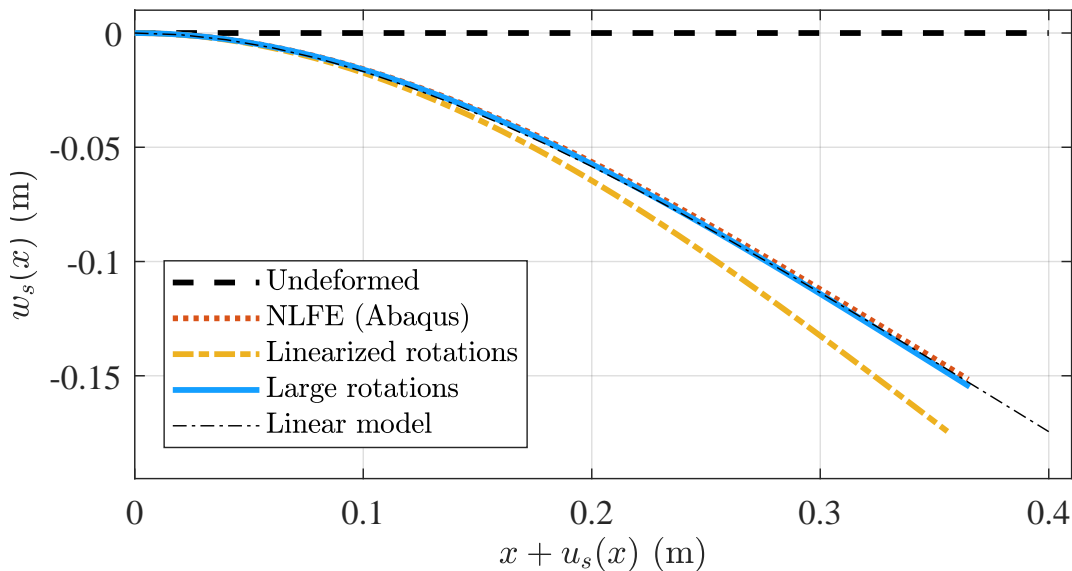


Figure 7: Static deformed shape comparison: HiFleW (linearized and large rotations) vs NLFE (ABAQUS).

Even though both versions of the nonlinear model tested in HiFleW capture the coupling behavior between axial and transverse displacements, the one with linearized rotations deviates drastically from the reference solution, in particular by overestimating vertical deflections. In fact, the tip deflection is equal to the analytical prediction for linear cantilever beams. The main reason is that if the third-order terms are neglected in the curvature expressions, there remain non-linear effects coupling different degrees of freedom but not geometrical stiffening in pure bending, which is derived from terms such as $v''v^2$ and $w''w^2$ in the potential energy expression.

Nevertheless, a slight difference still persists between the HiFleW solution and the reference solution. This could be attributed to the considerable deflection induced by the tip mass. In such cases, higher-order terms should naturally be retained in the equations of motion to enhance accuracy. In order to quantify this effect, and thus to determine the limitations of the present nonlinear structural model, the nonlinearity level is next modified by varying the value of the added tip mass, as was done experimentally in [24]. In Fig. 8 a), simulations with HiFleW are compared to NLFE and to the aforementioned experimental results. Fig. 8

b) displays the relative difference between experimental and computational tip deflection at equilibrium. As expected, the proposed model in HiFleW significantly outperforms the linear model but deviates from the experimental solution as the maximum deflection increases. Nevertheless, the relative error remains as low as 5% for deflections below 45% of beam span. This degree of accuracy is deemed satisfactory in the context of flexible wing studies, since such deflection levels would not be reached in practice. This justifies the practical use of the relatively simple beam model presented here instead of a geometrically-exact one [15].

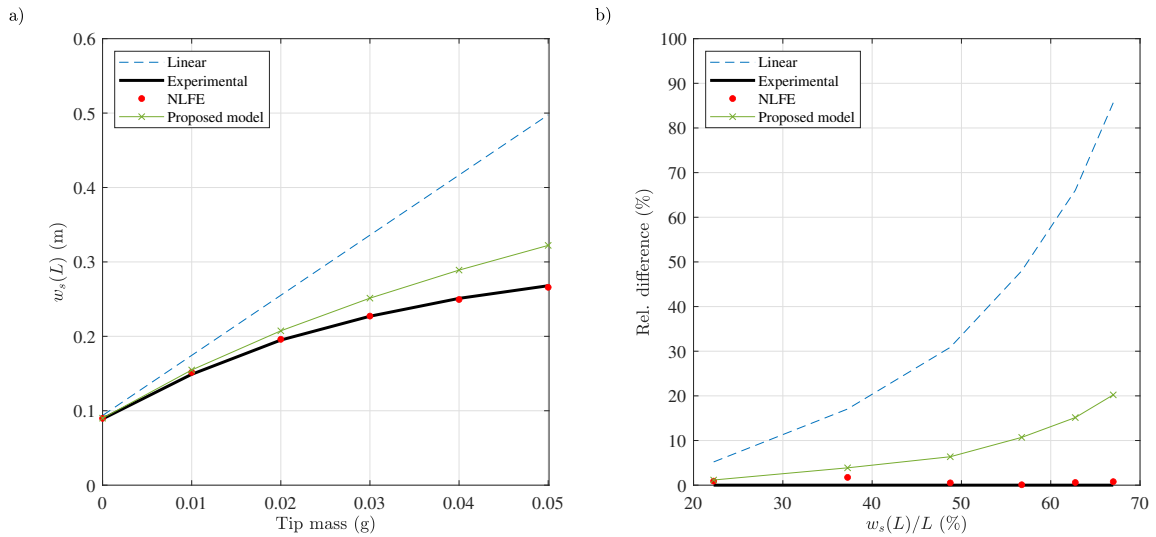


Figure 8: Comparison of different simulation methodologies: a) transverse tip displacement as a function of the added mass, b) relative difference to experimental measurements.

3.2. Dynamic test case on a linear beam

In order to investigate flutter and mode coalescence, an accurate prediction of modal characteristics is important. Thus, in this section, the first few linear natural frequencies of the previous straight beam structure are computed with HiFleW and compared to values obtained through well known formulas for Euler-Bernoulli beams. This is done in Table 2 for the first four modes of each kinematic variable. It follows that 6 shape functions for (u, v, w, ϕ) in the Rayleigh-Ritz approximation are sufficient for a good approximation of the first three linear natural frequencies of each variable. The modes are here-above uncoupled due to the symmetry of the cross-section, but this need not be the case in general.

Mode type	Theo.	HiFleW	Mode type	Theo.	HiFleW
	1.266×10^2	1.266×10^2		2.025	2.025
transverse	7.932×10^2	7.932×10^2	transverse	12.69	12.69
(<i>v</i>)	2.221×10^3	2.222×10^3	(<i>w</i>)	35.54	35.55
	4.352×10^3	4.622×10^3		69.64	73.95
	3.134×10^3	3.134×10^3		2.216×10^3	2.216×10^3
longitudinal	9.402×10^3	9.402×10^3	torsion	6.648×10^3	6.649×10^3
(<i>u</i>)	1.567×10^4	1.569×10^4	(ϕ)	1.108×10^4	1.110×10^4
	2.194×10^4	2.250×10^4		1.551×10^4	1.591×10^4

Table 2: Natural frequencies (Hz) of the rectangular beam compared with theory [25]. The frequencies are obtained with 6 shape functions per kinematic variable.

As an illustration of coupled bending/torsion modes typical in wing structure, the Goland wing [26] described in Table 3 is now adopted. The natural frequencies of the system without aerodynamic forces are calculated with HiFleW and compared with the literature [27]. For the same geometric and material properties³, the first three natural frequencies obtained with HiFleW are 49.331 rad/s, 99.202 rad/s and 246,60 rad/s. These are strictly equal to the reported values.

L	c	m	mk_t^2	EI_ζ	GJ	e_η	x_A
m	m	kg/m	kg.m	N.m ²	N.m ²	m	m
6.096	1.8288	35.71	8.64	9.77×10^6	0.99×10^6	-0.183	0.146

Table 3: Goland wing data.

3.3. Aeroelastic test case

Aerodynamic forces acting on the Goland wing are now accounted for. Local stability, function of the incoming airspeed, is assessed by performing complex eigenvalue analysis of Eq. (25) linearized about the static equilibrium state, which is simply $\mathbf{q} = \mathbf{0}$ when weight is ignored. In this section, structural damping is also neglected.

³Those given in [27] are slightly different from those of Table 3 used in the flutter simulation of Section 3.3.

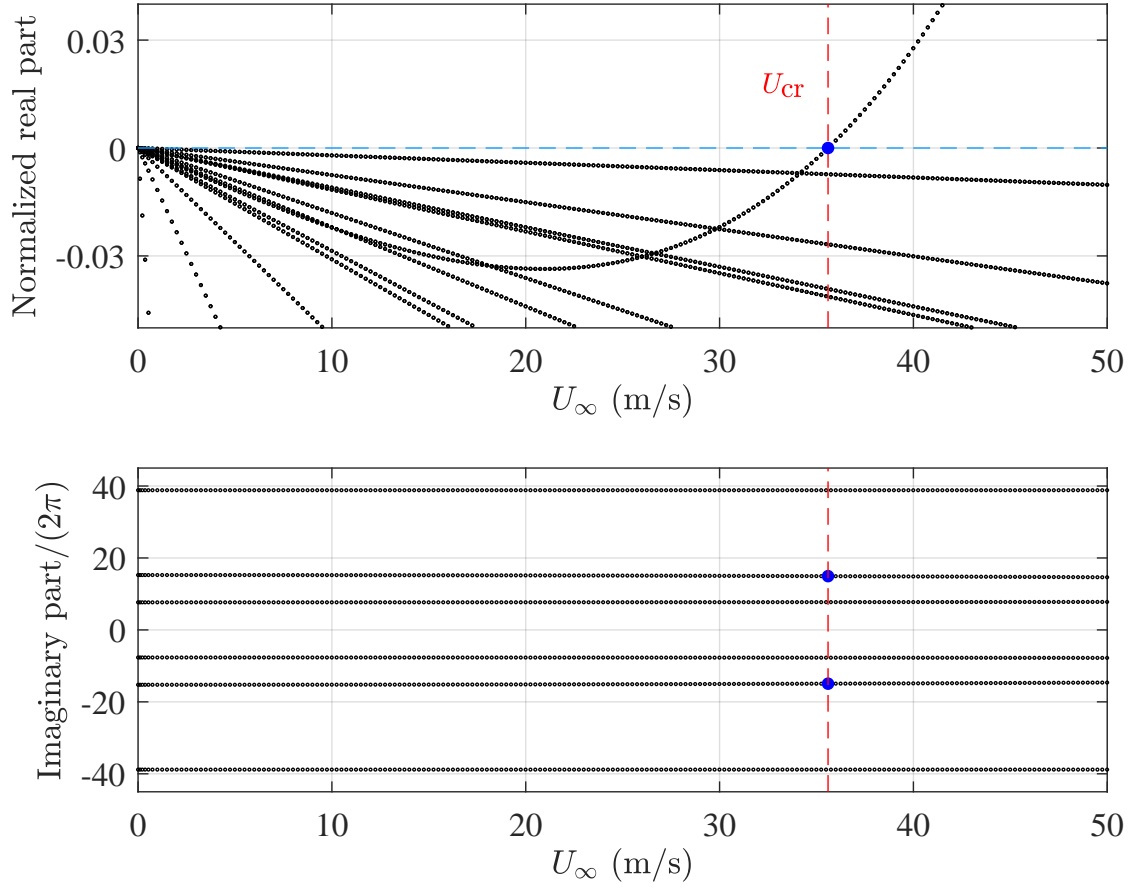


Figure 9: Bifurcation diagram for varying U_∞ , flutter occurs at $U_{cr} = 35.51$ m/s as indicated by (●) markers. Real parts of eigenvalues are normalized by the absolute value of their corresponding imaginary part.

Fig. 9 shows the evolution of the system's eigenvalues for $U_\infty \in [0, 50]$.⁴ Clearly, an unstable mode (associated to at least an eigenvalue having positive real part) exists for speeds beyond the critical value $U_{cr} = 35.51$ m/s. The unstable mode corresponds, in this case, to a complex-conjugate eigenvalue pair, which indicates a Hopf bifurcation leading to flutter. Furthermore, the LCO frequency in the immediate vicinity of the bifurcation is given by the imaginary part of the unstable mode, i.e.: $f_{cr} = 14.943$ Hz. Comparison with the literature and with simulations made with the GEBTAero code, in Table 4, shows a close correlation, thus

⁴As the imaginary parts increase rapidly from one eigenvalue to the next, only a close-up to the first six (out of the total 24) eigenvalues is shown in Fig. 9 for clarity.

validating the HiFleW toolbox for this application. It should be noted that the Golland wing is not particularly flexible and thus a nonlinear structural model is not mandatory to obtain similar results. A structure more akin to a solar HALE UAV wing is considered in the next section.

	Speed (m/s)	Frequency (Hz)
HiFleW	35.51	14.943
GEBTAero	35.09	14.983
Haddadpour et al. [28]	33.52	14.801

Table 4: Golland wing flutter speed and frequency for quasi-steady aerodynamics.

4. Application - Flutter mitigation by friction

This section considers the three-dimensional aeroelastic response of the full nonlinear structure, as presented in Sect. 2, consisting of the beam and the friction damper, the latter of which introduces a further source of nonlinearity into the system. The properties of the former, summarized in Table (5), are chosen to match the well-known flexible wing of [29], with a root pitch angle $\alpha_0 = 4^\circ$ (such as in [30] for instance). This results in a nonlinear static deformation dependent on wind speed U_∞ . All along this section, reference is made to an alternative configuration in which linear viscous damping (of coefficient ξ_D) is used as a dissipation mechanism in addition to, or rather than, frictional damping.

L	c	m	mk_t^2	EI_ζ	EI_η	GJ	e_η	x_A
m	m	kg/m	kg.m	N.m ²	N.m ²	N.m ²	m	m
16.0	1.0	0.75	0.1	2.0×10^4	4.0×10^6	1.0×10^4	0.0	0.25

Table 5: Patil wing data [29].

4.1. Friction damper parameters

The damper is required to be light relative to the total wing mass, in order to have a negligible effect over its static deflection. The damper-to-wing mass ratio is thus fixed to 1%. The damper stiffness is tuned in such a way as to target the unstable flutter mode of the structure. Its frequency is an implicit function of U_∞ , and it should ideally be adapted accordingly for optimal performance. For simplicity's sake, the

damper stiffness is kept constant and tuned to the frequency of the unstable mode at the critical speed (onset
of flutter) obtained in the damper's absence. This particular frequency is approximately 39.57 rad/s for the
wing described above and yields to $k_D = 188$ N/m.

4.2. Mitigation performance

4.2.1. Critical speed

The critical flutter speed is found through eigenvalue analysis of the system linearized about a static
equilibrium defined by the state $(\mathbf{q}, \dot{\mathbf{q}}) = (\mathbf{q}_0, \mathbf{0})$ solution of Eq. (25). The friction force has no effect on the
static equilibrium itself, but it affects its stability – and thus the flutter speed – through the state's Jacobian
matrix. To evaluate the impact of the damper on this regard, the critical speeds are predicted for different
attachment points along the wing span, using the numerical value: $\mu N = 0.5$ N for friction coefficient.
Regarding the regularization parameter ε , it is worthwhile to emphasize that the hyperbolic tangent function
has a quasi-linear behavior on the interval: $\dot{w}(x_D, t) - \dot{z}_D(t) \in [-\varepsilon, \varepsilon]$, which implies that a high value of this
parameter artificially introduces viscous damping into the system and modifies the critical speed. Hence,
while its specific value is irrelevant, ε must be chosen carefully in order to minimize this effect while also
providing sufficient smoothing to aid the numerical solvers. Following a convergence analysis -omitted here
for brevity-, the value $\varepsilon = 1 \times 10^{-4}$ is fixed in all that follows.

To assess the effectiveness of the friction damper, the same procedure is repeated for a viscous damper
with $\xi_D = 1.5$ kg/s. These computations yield the results presented in Fig. (10). As a first observation, one
notes that the friction damper has a small but noticeable effect on the critical speed, which can be considered
beneficial since the instability threshold is delayed regardless of the chosen damper position. The same can
be said about the viscous damper, which shows an identical behavior for attachment positions below 30%
of the wing span. Beyond this threshold, the viscous damper delays the instability the furthest. It should be
noticed however, that this Hopf bifurcation may be subcritical, implying the existence of periodic LCO for
speeds below U_{cr} . As such, a study of the LCO branches is crucial for determining the stabilizing value of
any damper.

4.2.2. LCO amplitude

With the Hopf bifurcation as a starting point, periodic LCO branches of Eq. (25) were computed numeri-
cally through a pseudo arc-length continuation algorithm implementing the harmonic balance method⁵ (see,

⁵To achieve solution convergence, 5 harmonics were sufficient with no friction, and 15 harmonics were needed for $\mu N = 1.5$ N.

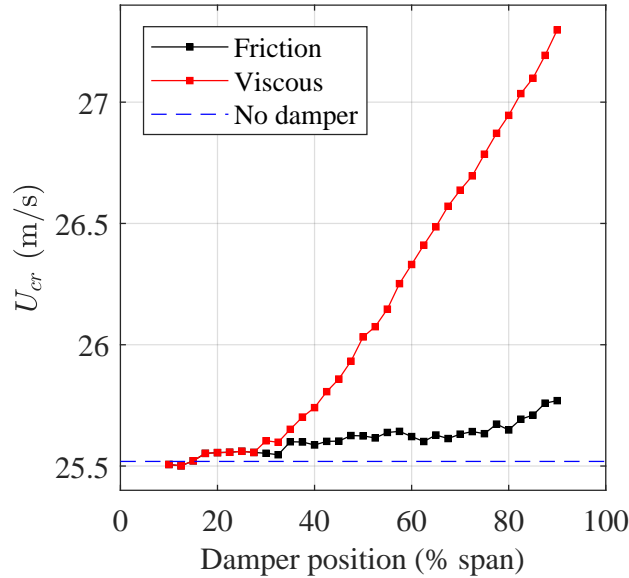


Figure 10: Critical speed as a function of damper position.

e.g., [31]). As an example, Fig. (11) shows the LCO obtained for $U_\infty = 26$ m/s in the absence of damper. The response mainly involves torsion and transverse bending in a lesser extent, characteristic of flutter. Through nonlinear coupling, the axial and lateral degrees of freedom also undergo periodic motion. The whole branch of solutions can be seen as the (—) curve in Fig. (12), where the subscript 'PP' denotes peak-to-peak amplitude. The bifurcation is subcritical, so there is an interval of U_∞ below the critical speed where a stable cycle and static equilibrium coexist. In practice, increasing speed past the critical point leads to jump to a large-amplitude cycle, rather than a gradual increase. It is important to note that the large torsion angles presented here are not the same as local angles of attack, which remain within the hypotheses introduced in Sect. (2.2).

Fig. (12) also groups results obtained with a friction damper, a viscous damper, and a combination of both. Considering first the viscous damper alone, it can be seen that the critical speed is delayed, as expected from Sect. 4.2.1. However, the bifurcation remains subcritical and the cycle amplitudes in the vicinity of U_{cr} remain large. In contrast, the friction damper alone shows a dramatically different behavior: for $\mu N = 0.5$ N, while the bifurcation is still subcritical, the amplitude jump is reduced to approximately one-quarter magnitude, and amplitudes remain small over some U_∞ -range greater than U_{cr} . Moreover, the bi-stability

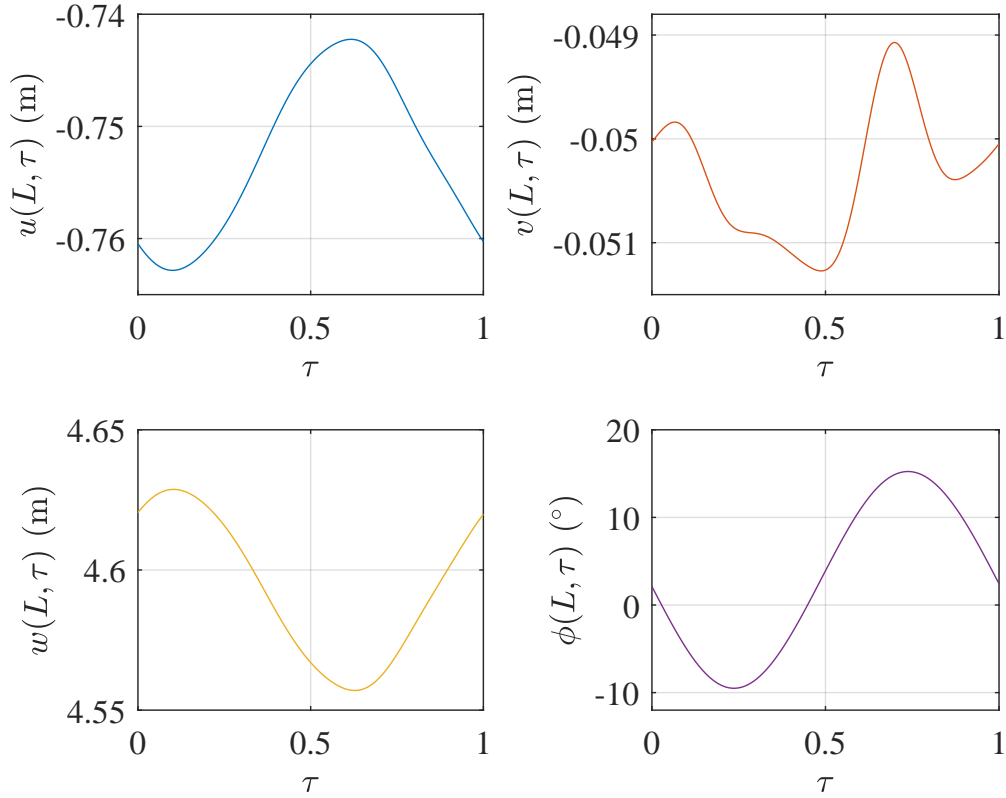


Figure 11: Beam tip motions over one period of LCO at $U_\infty = 26$ m/s (time τ is shown normalized by the oscillation period).

region for subcritical speeds is diminished. Nevertheless, a second amplitude jump appears in the LCO curve (at $U_\infty \approx 27.2$ m/s). Increasing the value of μN to 1.5 N eliminates the second amplitude jump, but at the cost of increasing the magnitude of the first one considerably; however, the resulting amplitudes remain smaller when compared to the viscous-damper case. When both dissipation mechanisms work together, the resulting curve is a compromise between the two: only an initial, small-magnitude amplitude jump exists, followed by a smooth but rapid increase of LCO amplitudes with airspeed.

Interestingly, regardless of the damper configuration employed, the amplitudes always tend to those of the damper-less case for values of U_∞ well beyond the critical speed. This can be explained by considering that a damper is effective to the extent in which it can dissipate the energy which is provided by the main structure. Since the attachment is linear and tuned to a given frequency, effective energy transfer to the damper can only occur in near internally-resonant conditions, i.e., if the LCO frequencies remain close to

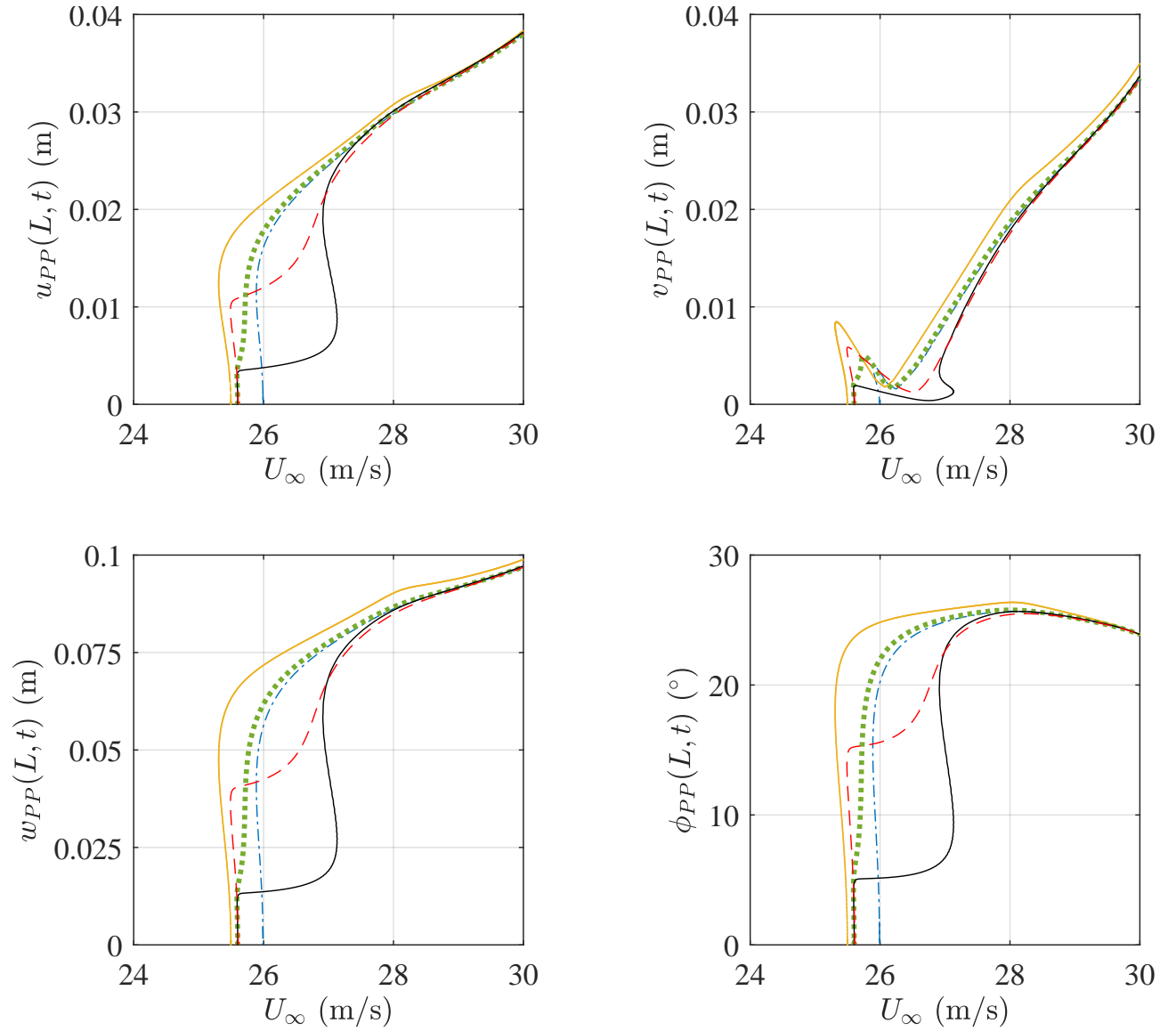


Figure 12: Peak-to-peak limit cycle amplitudes at beam tip for varying U_∞ , with damper located at: $x_D = 0.5L$. The curves correspond to the following (friction, viscous) damper configurations, with pairs in parentheses, giving the coefficients $(\mu N, \xi_D)$ in (N, kg/s): (—) (0,0), (—) (0.5,0), (- - -) (1.5,0), (- · - ·) (0,1.5) and (· · · ·) (1.5,1.5).

this value. As illustrated in Fig. 13, the energy dissipated by friction over one oscillation period attains a maximum and then decreases with further increases in U_∞ , which correlates directly with a sudden change in frequency away from the tuned value. This fact is, of course, a limitation to all tuned dampers, and could be

345

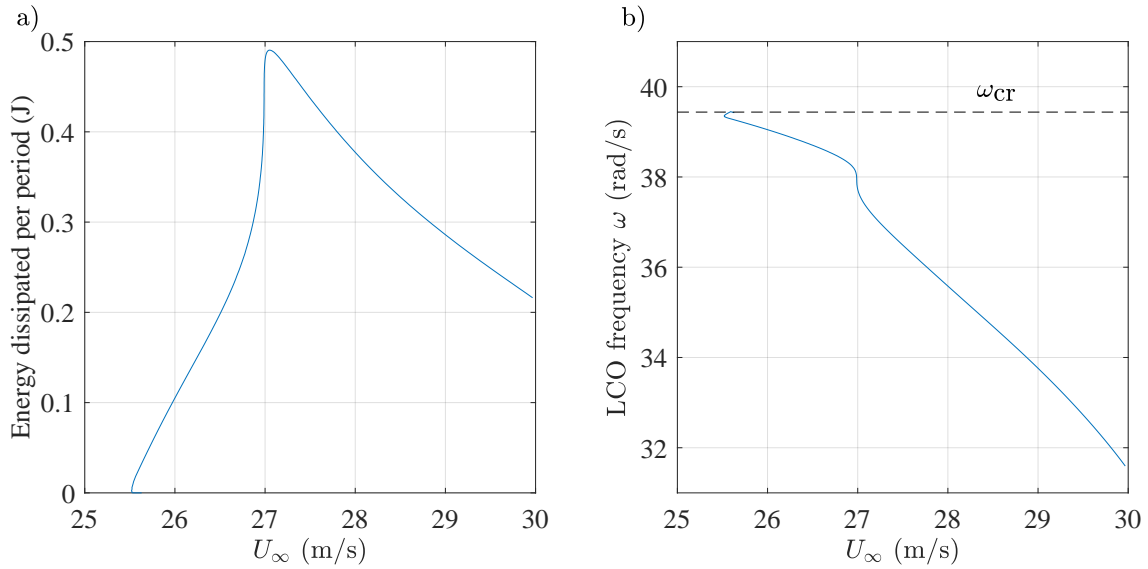


Figure 13: Evolution of LCO properties for varying U_∞ , given a friction damper at $x_D = 0.5L$ and $\mu N = 0.5$ N. a) Energy dissipated per period, b) LCO frequency.

remedied through the use of a nonlinear attachment, but this study is beyond the scope of the present paper.

5. Discussion

In this paper, the concept of a friction-based damper to mitigate limit cycle oscillations induced by flutter of flexible wings has been investigated. To this end, the HiFleW toolbox was developed, which incorporates a nonlinear beam model which improves on previous non-exact propositions by including moderate-rotation effects. While the resulting aeroelastic description is greatly simplified (most notably in regards to airflow-induced forces on the structure), it has proved sufficient to test the damper from a conceptual viewpoint, and the results obtained suggest that such a solution could be a viable alternative. Indeed, its performance with regard to limit cycle amplitude and bifurcation behavior is seen to be better than that of a linear viscous damper of equivalent dissipation capacities. Two important aspects to take into consideration for an optimal performance are the damper's attachment location on the wing and the damper's stiffness. The former plays a minor role on critical speed but also relates to the practical realization of such a device, while the second is crucial as it dictates the range of frequencies around which the dissipation will be effective. For solar HALE aircraft whose operation requires to elevate to high altitudes, decreasing speed might not be possible and

375 In turn, the trigonometric functions of angles ψ and θ can be expressed in terms of displacements as follows:

$$\begin{aligned}\cos(\psi) &= \frac{1 + u'}{\sqrt{(1 + u')^2 + v'^2}} \\ \sin(\psi) &= \frac{v'}{\sqrt{(1 + u')^2 + v'^2}} \\ \cos(\theta) &= \sqrt{\frac{(1 + u')^2 + v'^2}{(1 + u')^2 + v'^2 + w'^2}} \\ \sin(\theta) &= \frac{-w'}{\sqrt{(1 + u')^2 + v'^2 + w'^2}}\end{aligned}$$

References

- [1] T. E. Noll, S. D. Ishmael, B. E. Henwood, M. E. Perez-Davis, G. C. Tiffany, J. M. Madura, M. Gaier, J. M. Brown, T. Wierzbanski, Technical findings, lessons learned, and recommendations resulting from the helios prototype vehicle mishap, Tech. rep., NASA communication (2007).
- 380 [2] M. J. Patil, D. H. Hodges, Flight dynamics of highly flexible flying wings, *Journal of Aircraft* 43 (6) (2006) 1790–1799. doi:10.2514/1.17640.
- [3] C. M. Shearer, C. E. Cesnik, Nonlinear flight dynamics of very flexible aircraft, *Journal of aircraft* 44 (5) (2007) 1528–1545. doi:10.2514/1.27606.
- [4] A. del Carre, A. Muñoz-Simón, N. Goizueta, R. Palacios, Sharp: A dynamic aeroelastic simulation
385 toolbox for very flexible aircraft and wind turbines, *Journal of Open Source Software* 4 (44) (2019) 1885. doi:10.21105/joss.01885.
- [5] B. Kirsch, O. Montagnier, E. Bénard, T. M. Faure, Tightly coupled aeroelastic model implementation dedicated to fast aeroelastic tailoring optimisation of high aspect ratio composite wing, *Journal of Fluids and Structures* 94 (2020) 102930. doi:10.1016/j.jfluidstructs.2020.102930.
- 390 [6] L. Librescu, P. Marzocca, Advances in the linear/nonlinear control of aeroelastic structural systems, *Acta Mechanica* 178 (2005) 147–186. doi:10.1007/s00707-005-0222-6.
- [7] A. Malher, C. Touzé, O. Doaré, G. Habib, G. Kerschen, Flutter Control of a Two-Degrees-of-Freedom Airfoil Using a Nonlinear Tuned Vibration Absorber, *Journal of Computational and Nonlinear Dynamics* 12 (5) (2017) 051016. doi:10.1115/1.4036420.

- 395 [8] J. García Pérez, A. Ghadami, L. Sanches, G. Michon, B. I. Epureanu, Data-Driven Optimization for Flutter Suppression by Using an Aeroelastic Nonlinear Energy Sink, SSRN Electronic Journal (2022). [doi:10.2139/ssrn.4019600](https://doi.org/10.2139/ssrn.4019600).
- [9] C. Escudero, Contrôle passif des instabilités aéroélastiques des ailes d'avion par ajout d'oscillateurs non linéaires, Ph.D. thesis, ISAE-Supaero (2021).
- 400 [10] W. Whiteman, A. Ferri, Suppression of bending-torsion flutter through displacement-dependent dry friction damping, in: 37th Structure, Structural Dynamics and Materials Conference, Salt Lake City, USA, 1996, pp. 1578–1584. [doi:10.2514/6.1996-1489](https://doi.org/10.2514/6.1996-1489).
- [11] A. Sinha, J. H. Griffin, Friction damping of flutter in gas turbine engine airfoils, *Journal of Aircraft* 20 (4) (1983) 372–376. [doi:10.2514/3.44878](https://doi.org/10.2514/3.44878).
- 405 [12] A. Vizzaccaro, L. Salles, C. Touzé, Comparison of nonlinear mappings for reduced-order modelling of vibrating structures: normal form theory and quadratic manifold method with modal derivatives, *Nonlinear Dynamics* 103 (4) (2020) 3335–3370. [doi:10.1007/s11071-020-05813-1](https://doi.org/10.1007/s11071-020-05813-1).
- [13] C. Howcroft, R. G. Cook, S. A. Neild, M. H. Lowenberg, J. E. Cooper, E. B. Coetzee, On the geometrically exact low-order modelling of a flexible beam: formulation and numerical tests, *Proceedings of the Royal Society A: Mathematical, Physical and Engineering Sciences* 474 (2216) (2018) 20180423. [doi:10.1098/rspa.2018.0423](https://doi.org/10.1098/rspa.2018.0423).
- 410 [14] D. Tang, E. Dowell, Effects of geometric structural nonlinearity on flutter and limit cycle oscillations of high-aspect-ratio wings, *Journal of Fluids and Structures* 19 (3) (2004) 291–306. [doi:10.1016/j.jfluidstructs.2003.10.007](https://doi.org/10.1016/j.jfluidstructs.2003.10.007).
- 415 [15] D. H. Hodges, A mixed variational formulation based on exact intrinsic equations for dynamics of moving beams, *International Journal of Solids and Structures* 26 (11) (1990) 1253–1273. [doi:10.1016/0020-7683\(90\)90060-9](https://doi.org/10.1016/0020-7683(90)90060-9).
- [16] A. Givois, A. Grolet, O. Thomas, J.-F. Deü, On the frequency response computation of geometrically nonlinear flat structures using reduced-order finite element models, *Nonlinear Dynamics* 97 (2) (2019) 1747–1781. [doi:10.1007/s11071-019-05021-6](https://doi.org/10.1007/s11071-019-05021-6).
- 420

- [17] N. Di Palma, B. Chouvion, F. Thouverez, Parametric study on internal resonances for a simplified nonlinear blade model, *International Journal of Non-Linear Mechanics* 141 (2022) 103941. doi: [10.1016/j.ijnonlinmec.2022.103941](https://doi.org/10.1016/j.ijnonlinmec.2022.103941).
- [18] D. Hodges, E. Dowell, Nonlinear equations of motion for the elastic bending and torsion of twisted nonuniform rotor blades, Tech. rep., NASA-TN-D-7818, NASA communication (1974).
425
- [19] J. Sicard, J. Sirohi, An analytical investigation of the trapeze effect acting on a thin flexible ribbon, *Journal of Applied Mechanics* 81 (01 2014). doi: [10.1115/1.4028781](https://doi.org/10.1115/1.4028781).
- [20] B. D. Coleman, E. H. Dill, M. Lembo, Z. Lu, I. Tobias, On the dynamics of rods in the theory of Kirchoff and Clebsch, *Archive for Rational Mechanics and Analysis* 121 (4) (1993) 339–359. doi: [10.1007/BF00375625](https://doi.org/10.1007/BF00375625).
430
- [21] Y. C. Fung, *An introduction to the theory of aeroelasticity*, Dover Publications, 2008.
- [22] D. H. Hodges, G. A. Pierce, *Introduction to Structural Dynamics and Aeroelasticity*, 2nd Edition, Cambridge Aerospace Series, Cambridge University Press, 2011. doi: [10.1017/CB09780511997112](https://doi.org/10.1017/CB09780511997112).
- [23] S. Quaegebeur, N. Di Palma, B. Chouvion, F. Thouverez, Exploiting internal resonances in nonlinear structures with cyclic symmetry as a mean of passive vibration control, *Mechanical Systems and Signal Processing* 178 (2022) 109232. doi: [10.1016/j.ymsp.2022.109232](https://doi.org/10.1016/j.ymsp.2022.109232).
435
- [24] Z. Beléndez, C. Neipp, A. Beléndez, Numerical and experimental analysis of a cantilever beam: a laboratory project to introduce geometric nonlinearity in mechanics of materials, *International Journal of Engineering Education* 19 (2003) 885–892.
- [25] R. D. Blevins, R. Plunkett, Formulas for natural frequency and mode shape, *Journal of Applied Mechanics* 47 (2) (1980) 461. doi: [10.1115/1.3153712](https://doi.org/10.1115/1.3153712).
440
- [26] M. Goland, The flutter of a uniform cantilever wing, *Journal of Applied Mechanics* 12 (4) (1945) A197–A208. doi: [10.1115/1.4009489](https://doi.org/10.1115/1.4009489).
- [27] J. Banerjee, H. Su, C. Jayatunga, A dynamic stiffness element for free vibration analysis of composite beams and its application to aircraft wings, *Computers & Structures* 86 (6) (2008) 573–579. doi: [10.1016/j.compstruc.2007.04.027](https://doi.org/10.1016/j.compstruc.2007.04.027).
445

- [28] H. Haddadpour, R. Firouz-Abadi, Evaluation of quasi-steady aerodynamic modeling for flutter prediction of aircraft wings in incompressible flow, *Thin-Walled Structures* 44 (9) (2006) 931–936. [doi:10.1016/j.tws.2006.08.020](https://doi.org/10.1016/j.tws.2006.08.020).
- 450 [29] M. Patil, Nonlinear aeroelastic analysis, flight dynamics, and control of a complete aircraft, Ph.D. thesis, Georgia Institute of Technology (1999).
- [30] J. Murua, R. Palacios, J. Graham, Assessment of wake-tail interference effects on the dynamics of flexible aircraft, *AIAA Journal* 50 (7) (2012) 1575 – 1585. [doi:10.2514/1.J051543](https://doi.org/10.2514/1.J051543).
- [31] R. Alcorta, B. Chouvion, O. Montagnier, Dynamics of a non-linear jeffcott rotor in supercritical regime, *International Journal of Non-Linear Mechanics* 148 (2023) 104272. [doi:10.1016/j.ijnonlinmec.2022.104272](https://doi.org/10.1016/j.ijnonlinmec.2022.104272).
- 455 [32] J. Jiang, S. Ho, N. Markle, N. W. G. Song, Design and control performance of a frictional tuned mass damper with bearing–shaft assemblies, *Journal of Vibration and Control* 25 (12) (2019) 1812–1822. [doi:10.1177/1077546319832429](https://doi.org/10.1177/1077546319832429).
- 460 [33] E. Bachy, E. Sadoulet-Reboul, G. Chevallier, N. Peyret, C. Arnould, E. Collard, Vibration absorption device, especially for an air vehicle member, patent n°WO2023104799 (A1) (2023).